Available online at www.sciencedirect.com
SCIENCE DIRECT®
Journal of Solid State Chemistry 178 (2005) 629–637
JOURNAL OF SOLID STATE CHEMISTRY
www.elsevier.com/locate/jssc

Structural, transport, and magnetic properties of $R\mathrm{MnO_3}$ perovskites (R = La, Pr, Nd, Sm, ^{153}Eu, Dy)

B. Dabrowski[a], S. Kolesnik[a,*], A. Baszczuk[b], O. Chmaissem[a], T. Maxwell[a], J. Mais[a]

[a]*Department of Physics, Northern Illinois University, Room 101, Faraday West, Normal Road, DeKalb, IL 60115, USA*
[b]*Institute of Low Temperature and Structure Research, Polish Academy of Sciences, Wroclaw, Poland*

Received 25 October 2004; received in revised form 29 November 2004; accepted 3 December 2004

Abstract

Structural, magnetic, and high-temperature thermogravimetric and resistive properties of stoichiometric $R\mathrm{MnO_3}$ (R = La, Pr, Nd, Sm, and Dy) and isotopically pure $^{153}\mathrm{EuMnO_3}$ perovskites have been studied. The structural parameters of $^{153}\mathrm{EuMnO_3}$ from neutron powder diffraction have been found to perfectly correlate with those for the other $R\mathrm{MnO_3}$ compounds. Resistivity measurements within a wide temperature range 300–1400 K have provided the characteristic temperatures of the nucleation of the orbitally disordered phase and the Jahn-Teller ordering transitions. We have confirmed a linear dependence of these characteristic temperatures on the average R–O bond angle $\langle\cos^2\theta\rangle$. We argue that the tolerance factor that is linearly related to the average of $\cos^2\theta$ is the most convenient parameter for reliable description of the structural and physical properties.

Keywords: Perovskites; Manganites; Structural properties; Tolerance factor

1. Introduction

Structural, transport, and magnetic properties of single-valent perovskite manganites $R\mathrm{Mn^{3+}O_3}$ (R = Rare Earth elements and Y) show great sensitivity to the magnitude of the tolerance factor $t = (R-\mathrm{O})/\sqrt{2}(\mathrm{Mn}-\mathrm{O}) < 1$; i.e., the geometric parameter that provides a measure of the mismatch between the equilibrium bond lengths of (R–O) and (Mn–O) [1]. The bond length mismatch is accommodated in the orthorhombic (O′) $R\mathrm{MnO_3}$ structure by rotation of the $\mathrm{MnO_{6/2}}$ octahedra resulting in bending of the equatorial (in the ab-plane) and azimuthal (along the c-axis) Mn–O–Mn bond angles θ away from 180° along all three crystallographic directions. In addition, lifting of the two-fold degeneracy of the Jahn-Teller $\mathrm{Mn^{3+}}$ ion in a high-spin t^3e^1 configuration leads to three different (Mn–O) bond lengths that are cooperatively ordered below temperature T_{JT} [2]. The ordered pattern exhibits alternating long (z^2)—short (x^2-y^2) bonds in the ab-plane and medium (x^2-y^2)–medium (x^2-y^2) length bonds along the c-axis [3]. This pattern leads to the A-type antiferromagnetism observed below the Neel temperature T_{N} with ferromagnetic superexchange interactions in the ab-plane and antiferromagnetic interactions along the c-axis for large ions R = La, Pr, Nd, and Sm [3]. More complex antiferromagnetic structures IC and E have been observed with decreasing size of the R = Eu, Gd, Tb, Dy, and Ho; i.e., with increased bending of the Mn–O–Mn bonds [4]. The complex antiferromagnetic structures with mixed ferromagnetic/antiferromagnetic superexchange interactions in the ab-plane have been accounted for in terms of the next-nearest-neighbor anisotropic interactions arising from the closer distance and the less screened interactions between the Mn ions [4].

Using high-temperature resistivity and thermoelectric power measurements on $R\mathrm{MnO_3}$ (R = La, Pr, and Nd) single-crystals, Zhou and Goodenough [1] inferred

*Corresponding author. Fax: +1 815 753 8565.
E-mail address: kolesnik@physics.niu.edu (S. Kolesnik).

0022-4596/$ - see front matter © 2005 Elsevier Inc. All rights reserved.
doi:10.1016/j.jssc.2004.12.006

recently nucleation and monotonic growth of the orbitally disordered phase above temperature $T^* < T_{JT}$ and a discontinuous transition at T_{JT} that signals transition to orthorhombic (O*) phase with dynamic J-T distortions. All observed transitions at T_{JT}, T^*, and T_N were shown to depend linearly on the average of the $\cos^2\theta$ [1]. In this communication we study structural, magnetic, and the high-temperature thermogravimetric and resistive properties of polycrystalline RMnO$_3$ (R = La–Dy) materials. The measured bond angles and bond lengths are used to correlate the structural and physical properties and to compare EuMnO$_3$ with other RMnO$_3$ (R = La–Dy) materials.

2. Experimental procedures and sample characterization

2.1. Synthesis

Polycrystalline RMnO$_3$ (R = La, Pr, Nd, Sm, ^{153}Eu, and Dy) samples were synthesized from stoichiometric mixtures of La$_2$O$_3$, Pr$_6$O$_{11}$, Nd$_2$O$_3$, Sm$_2$O$_3$, isotopically pure (98.8% enriched) ^{153}Eu$_2$O$_3$, Dy$_2$O$_3$, and MnO$_2$. Samples were processed using the solid-state reaction method and fired in air several times at various temperatures up to 1673 K (1400 °C) followed by natural furnace cooling. Under these conditions, no stoichiometric perovskite samples could be obtained. The stoichiometric samples were synthesized by firing twice with intermittent grinding in Ar (containing up to 20 ppm O$_2$) at 1673 K (1400 °C) for R = La and gradually lower temperatures for other R to 1573 K (1300 °C) for R = Dy. The dense samples appropriate for high-temperature resistivity measurements were made with embedded Pt electrodes by pressing small rectangular pellets in a cardboard container. Sample quality was checked at room temperature by X-ray powder diffraction on a Rigaku D/MAX Diffractometer using Cu$K\alpha$ radiation.

2.2. Thermogravimetric measurements

Thermogravimetric analysis (TGA) measurements were performed on a Cahn TG171 thermobalance to study the behavior of these materials as a function of temperature and oxygen partial pressure in order to understand the synthesis in more detail. For increased accuracy, samples as large as 1 g (consisting of small chunks) were heated in alumina crucibles suspended on sapphire rods. The weights of the samples were measured to a precision of 2 μg. Empty-crucible TGA runs were used for calibration and buoyancy corrections. The assignment of the absolute oxygen contents was confirmed by hydrogen reduction on the TGA balance to R_2O_3 and MnO.

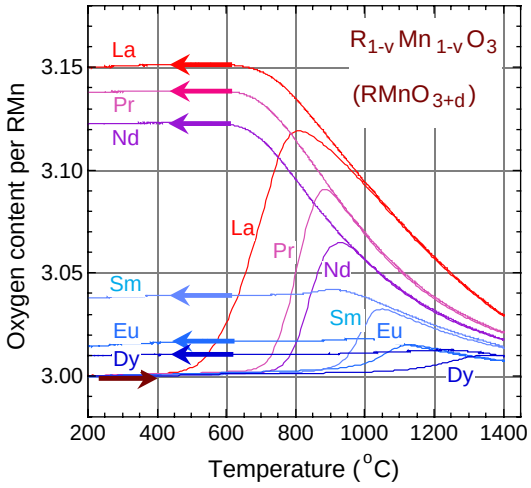

Fig. 1. Oxygen content, normalized to one formula unit of RMnO$_3$, measured during heating (2°/min) to 1670 K (1400 °C), holding for 4 h, and cooling (0.6°/min) to room temperature in 20% O$_2$/Ar using the single-phase perovskite samples obtained from synthesis in argon. The arrows indicate the direction of the temperature sweep.

Fig. 1 shows oxygen content, normalized to one formula unit of the RMnO$_3$, measured during heating (2°/min) to 1670 K (1400 °C), holding for 4 h, and cooling (0.6°/min) to room temperature in 20% O$_2$/Ar using the stoichiometric perovskite samples obtained from synthesis in argon. The stoichiometric samples begin to gain oxygen near 723 K (450 °C), 923 K (650 °C), 973 K (700 °C), 1123 K (850 °C), 1173 K (900 °C), and 1373 K (1100 °C), for R = La, Pr, Nd, Sm, Eu, and Dy, respectively. The increase of the oxygen content $3+d$ in the RMnO$_{3+d}$ formula to above 3 shown in Fig. 1 is caused by the development of vacancies on the R- and Mn-sites in equal proportions [5]. Clear correlation between the decreasing temperature of the cation vacancy formation and the increasing ionic size of R^{3+} is observed.

The onset temperatures of the cation vacancy formation seen in Fig. 1 are significantly higher then the typical temperatures of filling up the oxygen vacancies for manganites in air ~523–573 K (250–300 °C) [6]. Absence of the weight increases on TGA at these low temperatures supports the hydrogen reduction experiments and assures that the Ar-synthesized samples are stoichiometric in both the oxygen and cation content. The number of R- and Mn-vacancies $v = d/(3+d)$ in the formula of $R_{1-v}Mn_{1-v}O_3$ appearing in air is the largest for the biggest La ion and gradually decreases for smaller R. On further heating above ~1073–1373 K (800–1100 °C) samples begin to gradually loose oxygen. However, even at 1673 K (1400 °C) in air the samples exhibit a clear nonstoichiometry that progressively decreases from $d = 0.03$ for La to ~0.01 for Dy. Very good reproducibility of the data during heating and cooling at high temperatures indicates very fast kinetics

of cation-vacancy formation. On slow cooling the cation-vacancy formation stops near 873 K (600 °C) for La, Pr, and Nd at large values of $d = 0.15$, 0.14, and 0.12, respectively. For smaller R the kinetics of cation-vacancy formation is considerably slower and stops above 1173 K (900 °C) at lower values of $d = 0.04$, 0.015, and 0.01 for Sm, Eu, and Dy, respectively. TGA measurements shown in Fig. 1 demonstrate the necessity of performing synthesis as well as high-temperature physical and structural measurements in an oxygen-free atmosphere for obtaining reliable data for the stoichiometric samples.

2.3. Susceptibility, magnetization, and resistivity measurements

AC-susceptibility and static (DC) magnetization were measured using a Physical Property Measurement System 6000 (PPMS, Quantum Design). The "zero-field-cooled" (ZFC) magnetization was measured after cooling in zero magnetic field and switching on a magnetic field at a low temperature. The "field-cooled" (FC) magnetization was measured on cooling in the magnetic field. The remanent (rem) magnetization was measured after cooling in the magnetic field and switching the magnetic field to zero. The resistive properties of the samples were determined from standard 4-lead measurements performed using a home made apparatus between 300 and 1400 K. For temperatures $T < 400$ K, the PPMS resistive measurements were done using rectangular bars cut from pressed pellet samples whereas for high-temperature measurements rigid bars with embedded electrodes were used.

Magnetization and magnetic AC susceptibility are presented in Fig. 2(a, b) for RMnO$_3$. On cooling in the magnetic field (FC) we observe a step in the magnetization at the antiferromagnetic transition temperature T_N. At the same temperature, a sharp peak in the AC susceptibility can be observed. Below T_N, the magnetization displays a complicated nature due to the exchange interaction between Mn and R ions [7]. An additional peak in AC susceptibility for ^{153}EuMnO$_3$ can be observed at $T_{IC} = 49$ K, slightly above the antiferromagnetic transition at $T_N = 43$ K. These two temperatures are the boundaries of three magnetic phases: paramagnetic for $T > T_{IC}$, incommensurate antiferromagnetic (IC–AF) state for $T_{IC} > T > T_N$ and A-type antiferromagnetic (A–AF) for $T < T_N$ [4]. The step in the magnetization is observed at $T = T_N$, where the ferromagnetic component of the A-type antiferromagnetic phase is dominating.

In Fig. 2(c), the ZFC and FC magnetizations in magnetic fields of 1 and 70 kOe, and the remanent magnetization are shown for ^{153}EuMnO$_3$. One can observe that the remanent magnetization is almost equal to the FC magnetization in the A–AF state. This is a result of relatively strong magnetic anisotropy of this compound. The ZFC and FC magnetizations in 70 kOe follow closely each other. This is an indication that the ferromagnetic component is saturated in this high magnetic field.

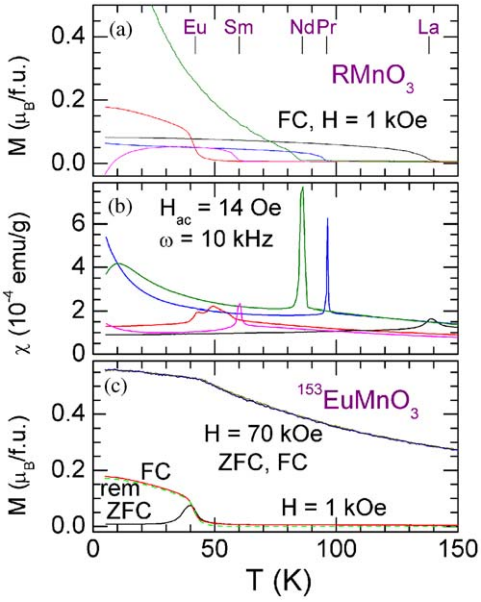

Fig. 2. (a) Magnetization and (b) magnetic AC susceptibility for RMnO$_3$. The short vertical lines mark the Neel temperatures T_N for each R. (c) "Zero-field cooled' (ZFC), "field-cooled" (FC) and remanent (rem) magnetization for ^{153}EuMnO$_3$.

Resistivity over a wide temperature range is presented in Fig. 3 for RMnO$_3$. The sharp drop of the resistivity at high temperatures can be associated with the transition from the cooperative Jahn-Teller ordered state (O′) to a phase with fluctuating J-T distortions (O*) [Fig. 3(a)]. To interpret the resistivity data we apply the method introduced by Zhou and Goodenough [1] based on phonon assisted conductivity model where $\rho/T \sim \exp(E_a/kT)$. Using this model, we have performed linear fits to the $\ln(\rho/T)$ vs. $1/T$ data (Fig. 3(b)) below and above the resistivity drop at T_{JT}. An exemplary fit for $R =$ La is presented in Fig. 3(b). The slope of this linear fit directly determines the value of the activation energy E_a. The temperature T^* below T_{JT}, for which the $\ln(\rho/T)$ vs. $1/T$ data start to deviate from linearity is defined as the onset of the orbitally disordered phase [1]. Table 1 shows the temperatures T^* and T_{JT}, and the E_a values below T^* and above T_{JT}. The E_a values below T^* are essentially constant across the RMnO$_3$ series. The E_a values above T_{JT} increase rapidly with decreasing size of R. The values of both quantities are similar to those previously determined for single crystals with $R =$ La, Pr, and Nd [1,4]. We notice that by using a wider temperature range of the resistivity measurement we were able to determine the temperatures T^* and T_{JT}, and the E_a values also for the smaller $R =$ Sm, Eu, and Dy.

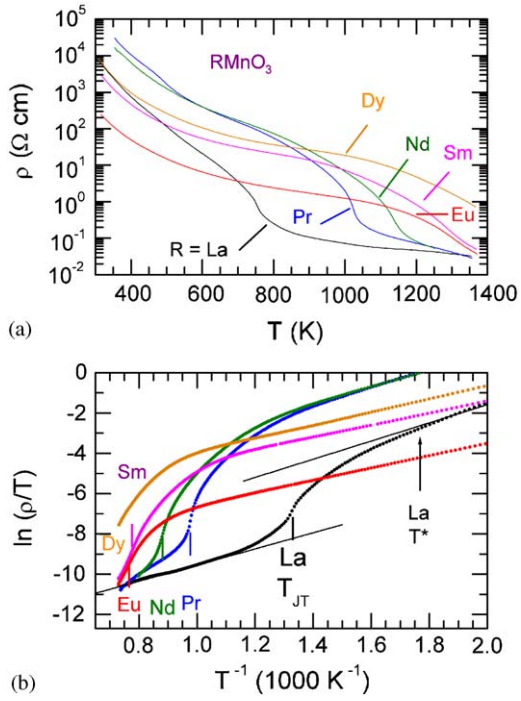

Fig. 3. (a) Resistivity over a wide temperature range for RMnO$_3$. (b) Logarithm of the ratio of resistivity over temperature vs. 1/T. The short vertical lines mark the Jahn-Teller transition temperatures T_{JT}. Long straight lines are linear fits (shown for R = La), from which the characteristic temperature T^* and activation energies were determined.

Fig. 4(a) shows transition temperatures T^* and T_{JT}, as a function of $\langle\cos^2\theta\rangle$ derived from the high-temperature resistivity measurements and the Mn–O–Mn bond angles measured for our RMnO$_3$ samples. As noted by Zhou and Goodenough [1] T^* and T_{JT} show striking linear variation with $\langle\cos^2\theta\rangle$ as shown in Fig. 4(a) extends to 1400 K. This variation of the onset of orbital-disorder fluctuations at T^* and the long-range orbital order–disorder transition at T_{JT} was discussed in terms of $T^* \sim T_{JT} \sim b^2$, where $b \sim \langle\cos\theta\rangle$ is the electron-energy transfer integral [1].

3. Crystal structure and tolerance factor

Time-of-flight neutron powder diffraction (NPD) data were collected on the Special Environment Powder Diffractometer at Argonne's Intense Pulsed Neutron Source. Diffraction data were collected at room temperature. High-resolution backscattering data ($2\theta = 144.85°$, Bank 1), and intermediate-resolution low-angle scattering data ($2\theta = 44°$, Bank 3), were analyzed using the Rietveld method with the General Structure Analysis System code GSAS (EXPGUI) suite [8]. The data sets used in the Rietveld refinement included d-spacing range between 0.5 and 4 Å. Background, peak width, absorption, and extinction parameters were refined, together with lattice parameters, atom positions, oxygen site occupancies, and isotropic temperature factors.

Fig. 5 shows raw NPD data and illustrates the results of the Rietveld refinement procedure for two members of the series NdMnO$_3$ and ^{153}EuMnO$_3$. The crystal structure of RMnO$_3$ was previously studied with neutron powder diffraction by Alonso et al. [9] for the series of compounds over a wide range of R^{3+} ion sizes. The compounds with R = Pr, Nd, Tb, Dy, Ho, Er and Y were prepared by soft-chemistry at 900–1000 °C from citrate precursors. For the smallest ions Y and Er a significant amount of a second phase with the hexagonal symmetry was observed. No structural studies with NPD were reported for EuMnO$_3$ because of the high neutron absorption of natural Eu. Our goal was to study the structural and magnetic properties of this intermediate size EuMnO$_3$ phase and compare them with the other members of the RMnO$_3$ series prepared under synthesis conditions that assure fully stoichiometric samples.

The NPD patterns for R = La, Pr, Nd, Eu, and Dy were collected at room temperature. All samples exhibit orthorhombic structure with the unit-cell parameters $a \approx \sqrt{2}a_p$, $b \approx \sqrt{2}a_p$ and $c \approx 2a_p$ (a_p is the ideal cubic perovskite lattice parameter). The refinements of the diffraction patterns carried out in the space group *Pbnm* confirmed the validity of this structural model. No significant deviation of the oxygen site occupancy from the values expected for stoichiometric RMnO$_3$ samples was observed. The final atomic coordinates, lattice parameters, oxygen site occupancies, and discrepancy factors obtained from structural refinement of the NPD data are given in Table 1. Table 2 contains the Mn–O–Mn bond angles and individual Mn–O and R–O bond lengths as well as their averages.

A uniform decrease of the unit cell volume with the size of R^{3+} is clearly observed from Table 1. Lattice parameters fulfill the $c/\sqrt{2} < a < b$ relation for all compounds. This is a typical relation observed for the O′-type structure for which severely distorted octahedral environment of the Mn^{3+} ion originating from a strong cooperative Jahn-Teller distortion causes the MnO$_{6/2}$ octahedron to expand along one of its directions in the a–b plane. The reduction of the R ionic size causes a decrease of the a and c lattice parameters whereas b slightly increases. The magnitudes of the unit-cell parameters are in accordance with Glazer's tilting scheme $a^-a^-c^+$ of the MnO$_{6/2}$ octahedra. The mismatch of the (R–O) and $\sqrt{2}$(Mn–O) bond lengths shown in Table 2 causes additional structural distortion emerging as a bending of the Mn–O–Mn bonds, $\theta \sim 155°$ for R = La. The reduction of the R ionic size further increases the bending of the Mn–O–Mn bonds to $\theta \sim 145°$ for R = Dy.

Table 1
Atomic coordinates, lattice parameters, oxygen site occupancies, and discrepancy factors obtained from structural refinement of the neutron powder diffraction data for RMnO$_3$

$R=$	La	Pr	Nd	Eu	Dy
T^* (K)	568	775	689	853	938
T_{JT} (K)	753	1023	1137	1310	
E_a (eV) for $T<T^*$	0.389	0.411	0.325	0.248	0.268
E_a (eV) for $T>T_{JT}$	0.346	0.779	1.18		
a (Å)	5.54051(42)	5.45000(13)	5.41678(51)	5.34370(16)	5.28016 (22)
b (Å)	5.74578(44)	5.82947(14)	5.85182(54)	5.83610(16)	5.84480(25)
c (Å)	7.69982(60)	7.58051(20)	7.54791(72)	7.46186(23)	7.37885(34)
V (Å^3)	245.121(33)	240.837(10)	239.25(4)	232.708(12)	227.722(17)
R (x y 1/4)					
X	−0.00755(2)	−0.0107(6)	−0.01370(32)	−0.0152(5)	−0.0180(4)
Y	0.04814(15)	0.0661(5)	0.07019(24)	0.07744(32)	0.08139(27)
B(Å^2)	0.41(3)	0.65(6)	0.35(5)	0.47(5)	0.35(4)
Mn (1/2 0 0)					
B(Å^2)	0.39(4)	0.28(6)	0.42(8)	0.23(9)	0.70(12)
O1 (x y 1/4)					
X	0.07506(20)	0.08556(35)	0.08901(35)	0.0974(5)	0.1017(9)
Y	0.48773(20)	0.51949(36)	0.47826(33)	0.4714(5)	0.4648(8)
n (O1)	1.024(4)	1.019(8)	1.005(7)	1.002(11)	1.007(2)
B (Å^2)	0.70(4)	0.52(5)	0.47826(33)	0.56(8)	0.45(9)
O2 (x y z)					
X	0.72610(15)	0.71512(26)	0.71242(27)	0.7055(4)	0.7013(6)
Y	0.30687(15)	0.31791(25)	0.31988(26)	0.3247(4)	0.3249(6)
Z	0.03881(10)	0.04333(20)	0.04472(19)	0.04845(28)	0.0518(5)
N (O2)	1.004(3)	1.008(7)	0.996(5)	1.025(9)	1.011 (9)
B (Å^2)	0.63(3)	0.56(4)	0.57(4)	0.60(4)	0.59(6)
Reliability factors					
R_p (%)	3.37	4.26	3.2	4.24	3
R_{wp} (%)	5.24	6.72	5.06	6.45	4.73
χ^2	2.095	1.151	1.212	1.400	1.548

The characteristic temperatures T^* and T_{JT} and activation energies E_a determined from high-temperature resistivity data are also presented.

4. Discussion

A reliable description of physical properties of perovskites in terms of the tolerance factor requires finding accurate sizes of the equilibrium interatomic bond lengths (R–O) and (Mn–O) from the NPD data. Table 2 shows all 12 individual R–O bonds for RMnO$_3$. The individual bonds show very large differences in lengths (~50%) and clearly split into two groups: eight short bonds of ~2.3–2.7 Å and four long bonds of ~3.2–3.7 Å. While the coordination of the R ion is obviously 12 in the cubic and slightly distorted perovskites, the definition of the bonding oxygen and, as such, the coordination of the R is a matter of uncertainty for severely distorted perovskites with several very long R–O bonds. For example, to calculate the average R–O, Alonso et al. [9] used 9 nearest-neighbor oxygen ions of R. In our previous publication [10] we have argued that the use of 12 coordinated R is justified for the (Sr,Ca)MnO$_3$ system where the transition from cubic ($\theta = 180^\circ$), through slightly distorted (tetragonal) to moderately distorted (orthorhombic, $\theta \sim 158^\circ$) structure is continuous [11]. Moreover, we have shown that the use of the geometrical average ($\langle R{-}O\rangle g = [\Pi_i (R{-}O)_I]^{1/12}, i = 1{-}12$) was preferred over the simple algebraic average ($\langle R{-}O\rangle a = [\Sigma_I (R{-}O)_i]/12, i = 1{-}12$) because it resulted in a shorter average bond for the distorted structures as it put less weight on the longer and weak bonds. Table 2 lists both the algebraic and geometrical averages for the R–O and Mn–O bonds using 12 and 6 coordinated R and Mn ions, respectively. The algebraic average $\langle R\text{–}O\rangle_I$ a gives an erroneous increase of the 12-coordinated R–O bonds from La to Nd. This increase is avoided for the geometrical average $\langle R\text{–}O\rangle g$ that also gives shorter bonds. However, the size of the average bond $\langle La\text{–}O\rangle g = 2.793$ Å is still markedly larger than the previously found value ($= 2.765$ Å) from the room temperature NPD of the La$_{1-x}$Sr$_x$MnO$_3$ system [12] over a range of compositions $x = 0.2{-}1$ with the cubic,

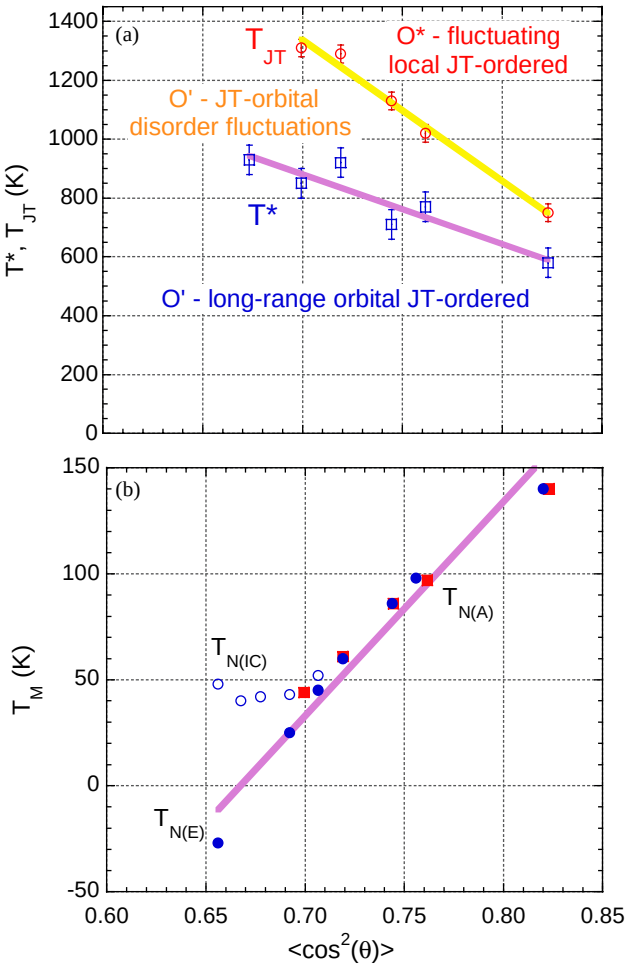

Fig. 4. (a) The characteristic temperatures T^* and T_{JT} determined from high-temperature resistivity data. (b) The magnetic temperatures T_M for $RMnO_3$ (filled squares present our data, filled circles, $T_M = T_N$ for A-type antiferromagnets and $T_M = -T_N$ for E-type antiferromagnets from Ref. [4], see text) and $T_{N(IC)}$ for IC-type antiferromagnets (from Ref. [4]).

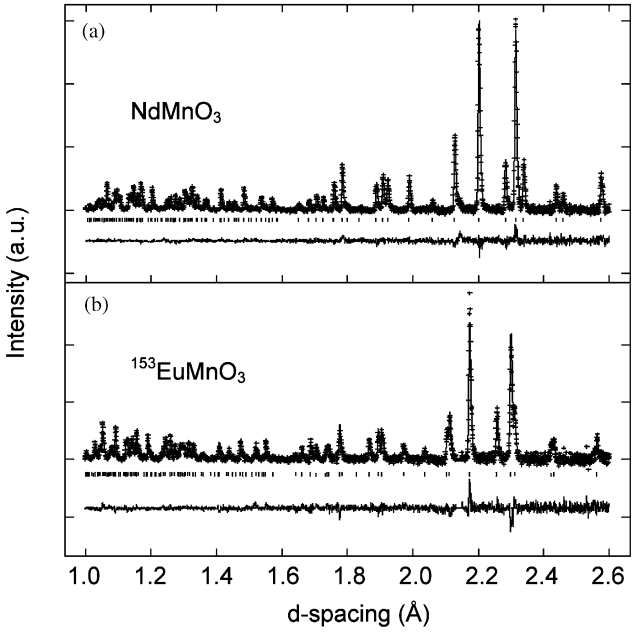

Fig. 5. Neutron powder diffraction patterns for: (a) $NdMnO_3$ and (b) for $^{153}EuMnO_3$. Crosses are the experimental data points. Short ticks indicate diffraction peaks. The lines in the bottom part of each panel show the difference between the experimental data and the best fit obtained using the Rietveld refinement method.

moderately distorted tetragonal, and the rhombohedral structures which do not exhibit the cooperative Jahn-Teller distortion. For $La_{1-x}Sr_xMnO_3$ in the range of compositions $x = 0-0.2$ with orthorhombic structures O* and O′, the difference of the individual La–O bonds as well as the average size of $\langle$La–O$\rangle g$ are increased, confirming that the presence of Jahn-Teller distortion of the $MnO_{6/2}$ octahedron causes these changes [13].

Table 2 shows that although the individual Mn–O bond lengths differ considerably among themselves (~15%), the averages $\langle$Mn–O$\rangle g$ and $\langle$Mn–O$\rangle a$ are quite similar and virtually do not change with the size of R. This is consistent with the fixed valence of Mn, confirming that the valence is a major parameter controlling the bond length. However, the value of $\langle$Mn–O$\rangle g = 2.02$ Å found here is larger than the previously derived value ($= 1.98$ Å) for the $La_{1-x}Sr_xMnO_3$ system over a range of compositions $x = 0.2-1$ [12]. Clearly, there is a considerable increase and differentiation of the Mn–O bond lengths resulting from the Jahn-Teller distortion for $x < 0.2$. In the following, for consistency with our previous findings, we will use the tolerance factor t defined by the equilibrium bonds $\langle R$–O$\rangle g$ and $\langle$Mn–O$\rangle g$ obtained from NPD measurements.

In Fig. 6 we show the tolerance factor t, the equatorial and azimuthal bond angles θ, and the average of $\cos^2\theta$ as a function of $\langle R$–O$\rangle g$. The magnitude of $t \sim 0.98$ for $R =$ La is larger than that found by Alonso et al. [9] ($t \sim 0.9$) mostly because of the difference in the definition of the average R–O bond lengths. All parameters t (Fig. 6(a)), the equatorial and azimuthal bond angles θ (Fig. 6(b)), and the average of $\cos^2\theta$ (Fig. 6(c)) display monotonic increase with $\langle R$–O$\rangle g$. The correlation between the structural and physical properties for perovskites is commonly described as a function of various parameters such as the R ionic size, the tolerance factor or the average of $\cos^2\theta$ [14]. As it can be seen from the nearly linear relation among these parameters in Fig. 6, all parameters are comparable and any one of them can be used for the single-valent perovskites of Mn^{3+}, provided the proper values are obtained from NPD measurements. For the mixed-valent ABO_3 perovskites, the ionic sizes of both A and B cations are necessary for a reliable description while the single parameters t or the average of $\cos^2\theta$ are sufficient in most cases when the size difference of the A-site ions is small. When the size difference of the A-site ions is

Table 2
Mn–O–Mn bond angles and individual Mn–O and *R*–O bond lengths as well as their algebraic and geometrical averages determined from the neutron diffraction data for $R\mathrm{MnO_3}$

Bond angles (deg), bond lengths (Å)	R = La	Pr	Nd	Eu	Dy
Mn–O1 (× 2)	1.9706(3)	1.9549(5)	1.9520(5)	1.94383(5)	1.9322(14)
Mn–O2 (× 2)	2.1835(9)	2.2172(15)	2.2234(15)	2.21988(5)	2.210(4)
Mn–O2 (× 2)	1.9036(9)	1.9095(15)	1.9109(15)	1.91152(4)	1.919(4)
$\langle$Mn–O$\rangle_a$	2.01924	2.0272	2.0288	2.0250	2.0204
$\langle$Mn–O$\rangle_g$	2.0158	2.0228	2.0242	2.0251	2.01610
Mn–O1–Mn	155.28	151.59	150.38	147.35	145.37
Mn–O2–Mn (× 2)	155.04	150.36	149.27	146.45	145.03
$\langle\cos^2\theta\rangle$	0.8230	0.7615	0.7445	0.6993	0.6734
R–O1	2.5669(14)	2.4729(33)	2.4523(24)	2.377(4)	2.329(5)
R–O1 (× 2)	2.4213(14)	2.370(4)	2.3626(23)	2.3169(34)	2.301(4)
R–O1	3.1634(15)	3.172(4)	3.1628(24)	3.172(4)	3.156(5)
R–O1	3.2524(14)	3.4527(32)	3.5086(25)	3.588(4)	3.658(5)
R–O2 (× 2)	2.6518(11)	2.6167(29)	2.5958(19)	2.5637(25)	2.523(4)
R–O2	2.4561(10)	2.4050(26)	2.3887(19)	2.3391(28)	2.307(4)
R–O2 (× 2)	2.7047(10)	2.6299(22)	2.6198(17)	2.5838(24)	2.569(4)
R–O2 (× 2)	3.3968(10)	3.5420(27)	3.5813(20)	3.6342(27)	3.660(4)
$\langle R$–O$\rangle_a$	2.8157	2.8183	2.8193	2.8061	2.7963
$\langle R$–O$\rangle_g$	2.7933	2.7845	2.7822	2.7616	2.7471

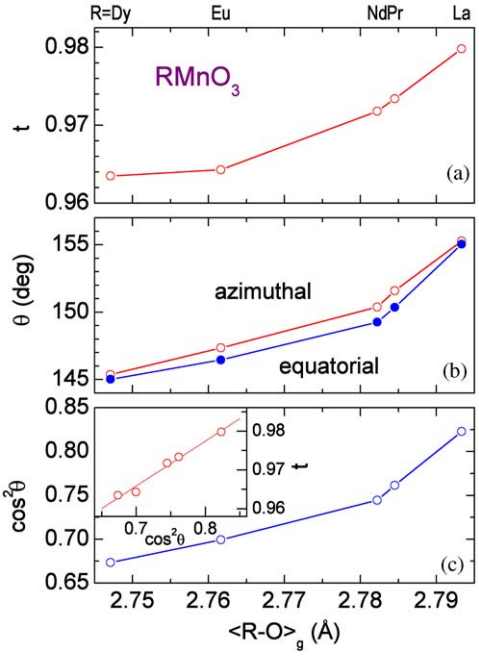

Fig. 6. (a) Tolerance factor t, (b) the equatorial and azimuthal bond angles θ, and (c) the average of $\cos^2\theta$ as a function of average bond-length $\langle R$–O$\rangle g$ for $R\mathrm{MnO_3}$. Inset shows the linear dependence of t with respect to $\cos^2\theta$.

large, the corrections in terms of the variance of sizes should be used [15].

By using the Goodenough–Kanamori rules of superexchange, the correlation of the magnetic transition temperatures T_M to the B–O–B bond-angle θ, $T_M \sim J = J_{90} - \langle\cos^2\theta\rangle(J_{90}-J_{180})$, has been clearly established for the single valent RBO_3 systems with $B = Fe^{3+}$ (t^3e^2) and Cr^{3+} (t^3) by means of superposition of 180° (antiferromagnetic, $J_{180}<0$) and 90° (ferromagnetic, $J_{90}>0$) interactions [16]. This formula predicts a change of the sign of superexchange interaction J at a critical angle θ_{crit} that depends on the values of J_{90} and J_{180}. A similar relationship between the Mn–O–Mn bond-angle and T_N (= 50–140 K) was observed for the $R\mathrm{MnO_3}$ perovskites with the R = Eu–La despite the opposite sign of interactions within the *ab*-plane and perpendicular to it [1,4]. Recently, Zhou and Goodenough [1,17] have argued that such a $T_N \sim \langle\cos^2\theta\rangle$ is anticipated for σ-bonding e_g orbitals based on antiferromagnetic interaction along the *c*-axis. In contrast to isotropic antiferromagnetic Fe^{3+} and Cr^{3+} perovskites, the Goodenough–Kanamori rules assign ferromagnetic interactions to 180° Mn–O–Mn bonds within the orbitally ordered *ab*-planes for the Jahn-Teller Mn^{3+} ion. While the superexchange interactions along the *c*-axis remain antiferromagnetic with increased bending of the Mn–O–Mn bonds for smaller R, the competing ferromagnetic and antiferromagnetic interactions within the *ab*-plane suppress *A*-type antiferromagnetic order. For the smallest R = Tb, Dy, and Ho the next-nearest-neighbor anisotropic interactions introduce complex antiferromagnetic structures IC and E with mixed ferromagnetic/antiferromagnetic interactions in the *ab*-plane [4].

Fig. 4 (b) shows magnetic transition temperatures as a function of $\langle\cos^2\theta\rangle$ for $R\mathrm{MnO_3}$ perovskites by taking $T_M = T_N$ for the *A*-type $R\mathrm{MnO_3}$ (R = La–Gd) antiferromagnets with FM interactions within the *ab*-plane

and $T_M = -T_N$ for the *E*-type $HoMnO_3$ antiferromagnet with the complex non-ferromagnetic interactions within the *ab*-plane [4]. Clearly the $T_M \sim \langle\cos^2\theta\rangle$ relation remains very well-satisfied for the $RMnO_3$ perovskites despite no immediate explanation in terms of the simple superposition of antiferromagnetic and ferromagnetic interactions within the *ab*-plane. The critical B–O–B bond-angle within the *ab*-plane where the magnetic interactions change from the FM to non-FM; i.e., the J_{ab} changes the sign is found at $\theta_{crit} \sim 145^\circ$. This value can be contrasted with $\theta_{crit} \sim 135^\circ$ that is obtained for the single-valent Mn^{4+} pyrochlores with isotropic interactions [18]. Decrease of T_N from 233 to 123 K with decrease of θ from 180 to 158° in $Sr_{1-x}Ca_xMn^{4+}O_3$ perovskites is consistent with this dependence, giving the extrapolated $\theta_{crit} \sim 147^\circ$ ($\langle\cos^2\theta_{crit}\rangle \sim 0.70$) [19].

To correlate structural and physical properties, the extraction of the individual bond angles θ and the average $\langle\cos^2\theta\rangle$ requires careful NPD study for every compound synthesized. Such procedure may be too troublesome considering the number of all possible combinations of several alkaline and rare earth's substituting on the perovskite *A*-site. Therefore, the tolerance factor that is linearly related to the average of $\cos^2\theta$ (see inset of Fig. 6(c)) is the most convenient parameter for use because it can be easily calculated once the ionic sizes of *A* and Mn (or the equilibrium *A*–O and Mn–O bond lengths) are tabulated for a given class of compounds. For example, we have previously found equilibrium *A*–O bond lengths for *A* = La, Pr, Ba, Sr, and Ca as well as the Mn^{3+}–O and Mn^{4+}–O bonds for manganites [12,20]. These bonds can be used customarily to find the tolerance factor of desired single-valent or mixed-valent composition. The calculated tolerance factor can than be used to predict structural and, in conjunction with the Goodenough–Kanamori rules of exchange interactions, the average magnetic properties of new single-valent perovskites as a function of composition without the need of their synthesis and the NPD study. If present, the intricacies of the real crystal structures such as the cation size variance, the exact vacancy distribution together with the absence or presence of Jahn-Teller effects, of orbital and/or spin order, of phase segregation phenomena, etc. make the use of the tolerance factor for predictions much too inaccurate. In addition, complexity of the superexchange and double-exchange interactions and the electron–phonon coupling prevents its usefulness to predict magnetic properties for mixed-valent compounds. However, we have shown that it is possible to extend definition of the tolerance factor to include the dependence on temperature and oxygen-content, and as such, provide design rules for synthesis of new manganites with desired chemical compositions, crystal structures, and the average magnetic and electronic properties for applications [13].

5. Summary

In summary, we have studied structural, magnetic, and high-temperature thermogravimetric and resistive properties of $^{153}EuMnO_3$ and compared them to the other $RMnO_3$ perovskites prepared under synthesis conditions that assure stoichiometric samples. By use of isotopically pure ^{153}Eu we have been able to perform neutron powder diffraction measurements on $^{153}EuMnO_3$ and determine the important structural parameters of this material. By performing resistivity measurements over a wide temperature range 300–1400 K while preserving the stoichiometry of $RMnO_3$ we have confirmed a linear dependence of the characteristic temperatures of the nucleation of the orbitally disordered phase and the Jahn-Teller ordering transitions on the average Mn–O–Mn bond angle $\langle\cos^2\theta\rangle$. We have argued that the tolerance factor that is linearly related to the average of $\cos^2\theta$ is the most convenient parameter for reliable description of the structural and physical properties because it can be easily calculated once the equilibrium *A*–O and Mn–O bond lengths are tabulated for a given class of $AMnO_3$ perovskites.

Acknowledgments

This work was supported by the NSF-DMR-0302617 and the US Department of Education.

References

[1] J.-S. Zhou, J.B. Goodenough, Phys. Rev. B 68 (2003) 144,406.
[2] J.B. Goodenough, Phys. Rev. 100 (1955) 564.
[3] J.B. Goodenough, Magnetism and the chemical bond, Wiley, New York, 1963.
[4] T. Kimura, S. Ishihara, H. Shintani, T. Arima, K.T. Takahashi, K. Ishizaka, Y. Tokura, Phys. Rev. B 68 (2003) 060403.
[5] J.A.M. Van Roosmalen, E.H.P. Cordfunke, R.B. Helmholdt, H.W. Zandbergen, J. Solid State Chem. 110 (1994) 100.
[6] E.N. Caspi, M. Avdeev, J.D. Jorgensen, S. Short, B. Dabrowski, O. Chmaissem, J. Mais, S. Kolesnik, J. Solid State Chem. 177 (2004) 1456.
[7] J. Hemberger, M. Brando, R. Wehn, V. Yu. Ivanov, A.A. Mukhin, A.M. Balbashov, A. Loidl, Phys. Rev. B 69 (2004) 064418.
[8] C. Larson, R.B. Von Dreele, Los Alamos National Laboratory Reports LAUR 86-748, 1994.
[9] J.A. Alonso, M.J. Martinez-Lope, M.T. Casais, M.T. Fernandez-Diaz, Inorg. Chem. 39 (2000) 917–923.
[10] B. Dabrowski, O. Chmaissem, M. Mais, S. Kolesnik, J.D. Jorgensen, S. Short, J. Solid State Chem. 170 (2003) 154.

[11] O. Chmaissem, B. Dabrowski, S. Kolesnik, J. Mais, D.E. Brown, R. Kruk, P. Prior, B. Pyles, J.D. Jorgensen, Phys. Rev. B 64 (2001) 134,412.
[12] O. Chmaissem, B. Dabrowski, S. Kolesnik, M. Mais, J.D. Jorgensen, S. Short, Phys. Rev. B 67 (2003) 094431.
[13] B. Dabrowski, X. Xiong, Z. Bukowski, R. Dybzinski, P.W. Klamut, J.E. Siewenie, C.W. Kimball, O. Chmaissem, J.D. Jorgensen, Phys. Rev. B 60 (1999) 7006.
[14] B. Dabrowski, O. Chmaissem, J. Mais, S. Kolesnik, Acta Phys. Pol. A 105 (2004) 45.
[15] L.M. Rodriguez-Martinez, J.P. Attfield, Phys. Rev. B 54 (1996) R15622.
[16] K. Mochida, S. Miyahara, J. Phys. Soc. Japan 28 (1970) 1188;
C. Boekema, F. Van Der Woude, G.A. Sawatzky, Int. J. Magnetism 3 (1972) 341.
[17] J.-S. Zhou, J.B. Goodenough, Phys. Rev. B 68 (2003) 054403.
[18] Y. Shimakawa, Y. Kubo, N. Hamada, J.D. Jorgensen, Z. Hu, S. Short, M. Nohara, H. Takagi, Phys. Rev. B 59 (1999) 1249.
[19] B. Dabrowski, O. Chmaissem, J. Mais, S. Kolesnik, J.D. Jorgensen, S. Short, Mater. Res. Soc. Symp. Proc. 718 (2002) 169.
[20] B. Dabrowski, O. Chmaissem, S. Kolesnik, J. Mais, J.D. Jorgensen, Physica C 387 (2003) 266.